A novel single-camera approach to large-scale, three-dimensional particle tracking based on glare-point spacing

Hou, Jianfeng; Kaiser, Frieder; Sciacchitano, Andrea; Rival, David E.

DOI
10.1007/s00348-021-03178-8

Publication date
2021

Document Version
Final published version

Published in
Experiments in Fluids

Citation (APA)
Hou, J., Kaiser, F., Sciacchitano, A., & Rival, D. E. (2021). A novel single-camera approach to large-scale, three-dimensional particle tracking based on glare-point spacing. *Experiments in Fluids*, *62*(5), Article 100. https://doi.org/10.1007/s00348-021-03178-8

Experiments in Fluids (2021) 62:100
https://doi.org/10.1007/s00348-021-03178-8

RESEARCH ARTICLE

A novel single-camera approach to large-scale, three-dimensional particle tracking based on glare-point spacing

Jianfeng Hou[1] · Frieder Kaiser[1] · Andrea Sciacchitano[2] · David E. Rival[1]

Received: 31 July 2020 / Revised: 7 February 2021 / Accepted: 3 March 2021

Abstract

A novel method for three-dimensional particle tracking velocimetry (PTV) is proposed that enables flow measurements in large volumes [$V = \mathcal{O}(10\ \mathrm{m}^3)$] using a single camera. Flow is seeded with centimeter-sized soap bubbles, when combined with suitable illumination, produce multiple glare points. The spacing between the two brightest glare points for each bubble is then utilized to reconstruct its depth. While the use of large soap bubbles comes at the expense of non-Stokesian behaviour, the excellent ray optics allow for large volume illumination when coupled with for instance pulsed LED banks. Possible error sources and the out-of-plane accuracy are discussed before the feasibility of the method is tested in an industrial-scale wind tunnel facility (test section of cross section 9.1 m × 9.1 m). In particular, the vortical structure in the wake of a 30%-scale tractor-trailer model at a 9° yaw angle is captured in a 4.0 m × 1.5 m × 1.5 m measurement volume. Long tracks of up to 80 time steps are extracted in three-dimensional space via a single perspective. The successful proof-of-concept confirms the potential of the novel approach for three-dimensional measurements in volumes of industrial scale.

Graphic abstract

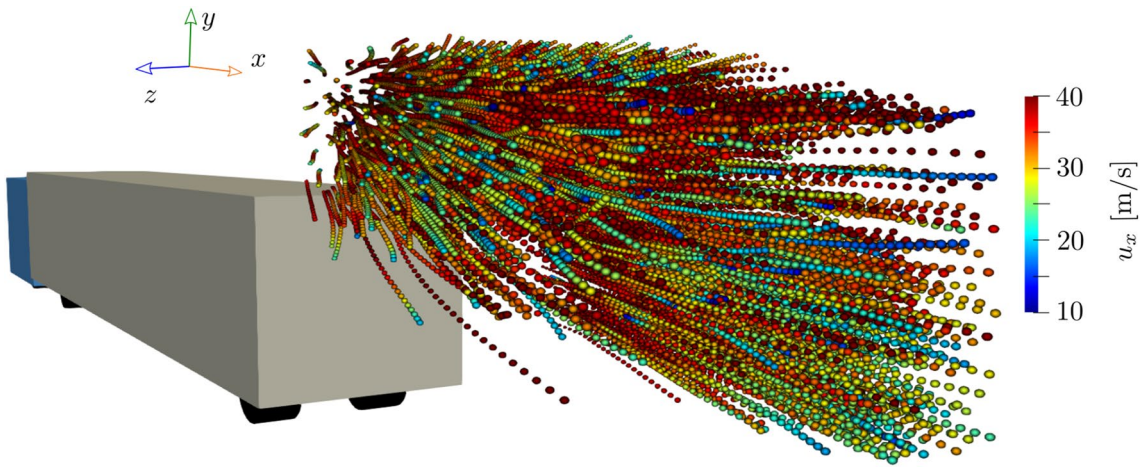

1 Introduction

Three-dimensional (3D) flow fields can be captured through a variety of multi-camera techniques including: 3D particle tracking velocimetry (3D-PTV) (Nishino et al. 1989; Maas et al. 1993), tomographic particle image velocimetry (tomo-PIV) (Elsinga et al. 2006), and most recently Shake-The-Box (Schanz et al. 2016). While such approaches have been optimized significantly in terms of accuracy and computational

✉ David E. Rival
d.e.rival@queensu.ca

[1] Department of Mechanical and Materials Engineering, Queen's University, Kingston, ON, Canada

[2] Department of Aerospace Engineering, Delft University of Technology, Delft, ZH, The Netherlands

Published online: 17 April 2021

cost since their introduction (see for instance Scarano 2012), such techniques traditionally suffer from two major drawbacks that limit their transfer to industrial applications. First, particularly in air, the low scattering efficiency of the traditional tracers (diameter $D = \mathcal{O}(1\ \mu\text{m})$) and the limited pulse energy of the light source limit the measurement volume of typical studies to $V < 100\ \text{cm}^3$ (Scarano et al. 2015). The limited size of the measurement volume is often accounted for by using scaled models of the geometry under consideration, which, in air, results in lower Reynolds numbers (Re). When large-volume measurements are attempted they are either realized by stitching multiple small measurement volumes together (see e.g. Sellappan et al. 2018) or by repeating stereo PIV measurements on many planes (see e.g. Suryadi et al. 2010). Michaux et al. (2018) automatized the process of capturing multiple stereo-PIV planes using three robotic arms to adjust the laser and the two cameras. To perform volumetric measurements at higher Re, measurements can be conducted in water (see e.g. Rosi and Rival 2018). However, due to the presence of the water–air interface, the camera calibration poses a significant challenge. Furthermore, experiments in water often come at high costs in terms of both the facility and the model. The second major issue preventing a broader application of 3D measurements particularly at large scales, is its complexity. Expensive multi-camera systems and challenging calibration are required. Such complex set-ups are rarely possible in non-laboratory conditions, and often too expensive and time-consuming for the result-oriented applications in industry. For instance in industrial applications as well as in large-scale wind tunnel testing, integral as well as point-measurement techniques remain the predominant tool for flow characterization. While well-established methods such as balances, pressure probes (single and multi-hole) and hot-wires provide a robust and affordable way to measure the aerodynamic loads or the local flow, these methods do not capture the coherent structures in the flow, which often are key to developing cause-effect relationships for such problems.

In air, the problem of limited light scattering for conventional particles ($D = \mathcal{O}(1\ \mu\text{m})$, Raffel et al. 2018) was tackled by testing larger tracer particles such as fog-filled soap bubbles ($D = \mathcal{O}(10\ \text{mm})$, Rosi et al. 2014), snowfall ($D = \mathcal{O}(1\ \text{mm})$, Toloui et al. 2014) and helium-filled soap bubbles (HFSB) ($D = \mathcal{O}(100\ \mu\text{m})$, Scarano et al. 2015). Larger tracer particles ($D > 100\ \mu\text{m}$) allow for measurement domains at the scale of cubic meters (see e.g. HFSB in 0.6 m^3 measurement volume, Huhn et al. 2017; HFSB in about 1.0 m^3 measurement volume, Bosbach et al. 2019). In addition, the enhanced light-scattering behaviour allows the use of less hazardous illumination sources such as searchlights (Toloui et al. 2014), LEDs (Buchmann et al. 2012; Huhn et al. 2017; Bosbach et al. 2019), and even natural light (Rosi et al. 2014). However, while large tracer particles enable the study of large-scale flows, for example the atmospheric surface layer, the growing tracer size introduces new challenges with regards to flow-tracking fidelity (Scarano et al. 2015; Raffel et al. 2018; Galler and Rival 2019) and thus limitations on the system resolution.

To reduce the system complexity for 3D measurements, single-camera approaches, as well as a compact multi-camera system, have been explored. Single-camera approaches based on defocusing were first suggested by Willert and Gharib (1992), who used three holes in the aperture to produce multiple images of the same particles on the camera sensor. Kao and Verkman (1994) introduced astigmatism to the optics of a microscope by a cylindrical lens to track the 3D motion of a single particle. Cierpka and Kähler (2012) adapted both principles (defocusing and astigmatism) successfully to enable 3D measurements in micro-PTV applications. Another promising single-camera approach demonstrated by Fahringer et al. (2015) and Zhao et al. (2019) is light-field PIV (LF-PIV), where the third dimension is reconstructed using the information gathered from a single plenoptic camera. However, the method is limited by depth resolution and elongation effects of the reconstructed particles. Moreover, Kurada et al. (1995) proposed a prism that enabled recording of three perspectives with a single camera chip. The prism was utilized by Gao et al. (2012) to perform volumetric measurements. As the former methods decrease the resolution of each view, Schneiders et al. (2018) introduced a coaxial volumetric velocimeter (CVV). The CVV integrates four cameras and the laser light illumination into a single module. Jux et al. (2018) combined the CVV with a robotic arm to automatically measure multiple subsets of a large measurement volume, providing time-averaged data in large volumes around complex geometries.

For the sake of simplifying the experimental effort, while still allowing time-resolved measurements in very large volumes, the present study introduces a novel approach for a single-camera 3D measurement technique and presents a first experiment to investigate the potential and the limitations of the approach. The approach makes use of the glare points on centimeter-sized soap bubbles to determine the out-of-plane position for each respective bubble, thus allowing for measurements in large volumes ($V = \mathcal{O}(10\ \text{m}^3)$), while maintaining a rather simple experimental set-up, as well as efficient image processing procedures.

In the present manuscript, the working principle is first introduced before the limitations of the method and possible error sources are discussed. The novel approach is then demonstrated via measurements in the wake of a 30%-scale tractor-trailer model at a 9° yaw angle in the 9.1 m × 9.1 m industrial wind tunnel at the National Research Council in Ottawa, Canada.

2 Methods

The present section outlines the working principle and the fundamental equations in Sect. 2.1, before Sect. 2.2 elaborates on possible error sources and how the accuracy of the out-of-plane position can be optimized. Thereafter, the experimental parameters of the present experiment (Sect. 2.3), and the detailed steps for post-processing are outlined (Sect. 2.4).

2.1 Working principle

Consider a spherical air-filled soap bubble of diameter $10\,\text{mm} < D_B < 25\,\text{mm}$ much larger than the soap film thickness $h = 0.3\,\mu\text{m} \ll D_B$. When the bubble is illuminated by a parallel light beam, a camera at an observation angle θ with respect to the illumination direction captures several reflections (glare points) on the bubble surface (van de Hulst and Wang 1991). For $\theta \approx 90°$ the two glare points of highest intensity are a result of external and an internal reflections, respectively (see Fig. 1a), whereas the remaining glare spots (typically at least one order of magnitude less intense) are ascribed to higher-order reflections (Dehaeck et al. 2005). For a small soap-film thickness, the relation for the glare-point spacing (D_G) between the two brightest glare points simplifies to

$$D_G = D_B \sin(\theta/2). \tag{1}$$

Hence, the glare-point spacing is directly proportional to the bubble diameter. If the light source and the camera are far away from the measurement volume, a constant θ can be assumed throughout the whole measurement volume. For $\theta = 90°$ this leads to $D_G = \sqrt{2}/2 D_B$, as shown in Fig. 1a.

Assuming that the bubbles remain spherical with constant diameter D_B, and that the variation of θ is negligible along the bubble's path, the image glare-point spacing (d_G) is related to D_B by the optical magnification factor M, as shown in Fig. 1b:

$$M = \frac{\sqrt{2} d_G}{D_B} = \frac{d_G}{D_G} = i/o, \tag{2}$$

where i is the image distance and o the object distance (Raffel et al. 2018). For $o \gg i$ the lens equation

$$f^{-1} = o^{-1} + i^{-1}, \tag{3}$$

leads to $f \approx i$, where f is the camera lens focal length. Equation (2) simplifies to

$$o = \frac{D_G f}{d_G}. \tag{4}$$

With Eq. (4), and for known bubble diameters $D_B = \sqrt{2} D_G$, the motion of a bubble in 3D space can then be extracted by a single camera.

2.2 Error sources and out-of-plane resolution

As for every measurement method, the proposed glare-point approach also has its limitations. The present section explores the most critical error sources and these effects might be mitigated.

The extraction of the out-of-plane position for each bubble requires knowledge about the bubble size (D_B). The error estimate for D_B propagates linearly into the estimate of o (Eq. (4)), and therefore also into derived quantities such as the velocity or the material acceleration. The optimal solution would be a bubble generator (currently in development) that produces equally-sized bubbles of known size. However, also alternate approaches are possible. For instance, if the illuminated region and the flow

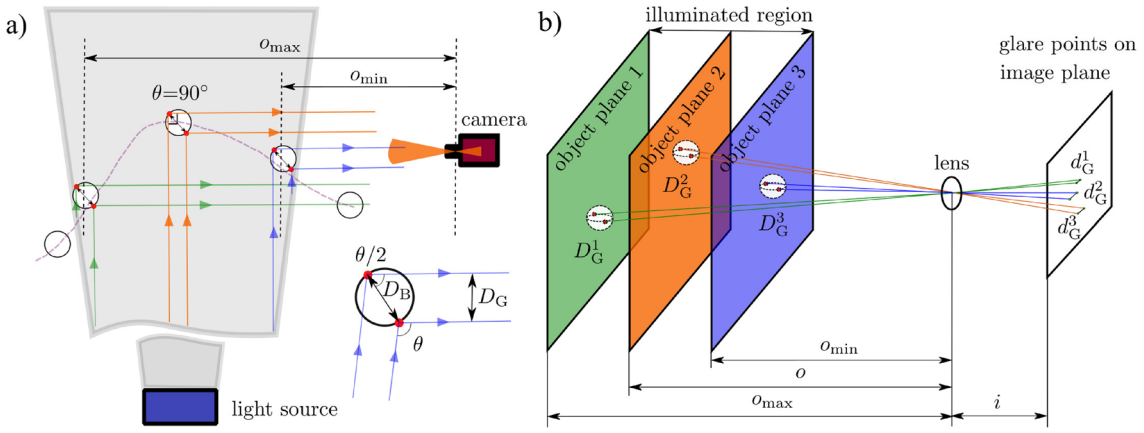

Fig. 1 **a** Imaging of soap bubble glare points (red dots) and the dependence of the glare-point spacing D_G on the light-source angle θ (bottom right). **b** As the bubble moves towards the camera (lens), the depth (object distance o) changes and leads to a change in the glare-point spacing d_G on the image plane

direction are known, D_B can be estimated as soon as the bubble first appears in the image. Alternatively, D_B can be estimated by a secondary view through the principle of photogrammetry. These details are outlined in Sect. 2.4.

The relatively large size of the soap bubbles leads to two issues. First, strong material accelerations can lead to periodic bubble deformation (Kornek et al. 2010) that decays slowly. The deformation will influence the glare-point spacing and therefore the estimate of depth. Note, however, that the periodic motion is visible in the time history of the glare points and the affected bubbles can easily be filtered from such an evaluation. The second problem is coupled to the non-Stokesian behaviour of the bubbles. While the Stokes drag applies to traditional tracers, very large bubbles will deviate from this regime (Clift et al. 1978). The effects of this deviation, however, can be modelled and compensated in the future (see e.g. Galler and Rival 2019). A correction of the extracted tracks using such models goes beyond the scope of the present manuscript and will be addressed in future work.

As for all single-camera approaches (see Sect. 1), the present method suffers from a limited resolution in the out-of-plane direction. In particular, the out-of-plane component is resolved by the difference between $d_G(o_{\min})$ and $d_G(o_{\max})$, where $o_{\max}$ is the maximum and $o_{\min}$ the minimum object distance, respectively. For a given measurement volume depth $o_{\max} - o_{\min}$, the value of

$$\Delta d_G = d_G(o_{\min}) - d_G(o_{\max}) = f D_G \left(\frac{1}{o_{\min}} - \frac{1}{o_{\max}} \right) = f D_G \frac{o_{\max} - o_{\min}}{o_{\max} o_{\min}}, \tag{5}$$

has to be maximized. To allow for bright images, a small f-number ($\mathcal{F}$) is preferred. As small $\mathcal{F}$ results in a limited depth-of-field (DOF), the limits of the measurement volume ($o_{\max}$ and $o_{\min}$) are set to the limits of acceptable image sharpness (Greenleaf 1950):

$$\begin{aligned} o_{\max} &= \frac{o_f f^2}{\mathcal{F}c\left(f^2/(\mathcal{F}c) - o_f\right)} \\ o_{\min} &= \frac{o_f f^2}{\mathcal{F}c\left(f^2/(\mathcal{F}c) - f + o_f\right)}, \end{aligned} \tag{6}$$

where o_f is the focus distance, and c is the circle of confusion that describes the acceptable blurriness of the image. The combination of Eqs. (5) and (6) leads to the simple expression

$$\Delta d_G = \frac{D_G \mathcal{F}c}{o_f f}(2o_f - f) \approx \frac{2 D_G \mathcal{F}c}{f}, \tag{7}$$

where in the last step $o_f \gg f$ is assumed. Equation (7) implies that shorter focal lengths will allow for better depth resolution. Note, however, that small f results in wide opening angles and thereby leads to a measurement volume that is shaped more like a truncated pyramid than that of a cuboid. Furthermore, for small f the measurement volume is located close to the camera, in turn possibly modifying the flow. For the present study $f = 60$ mm (AF Micro-Nikkor 60 mm f/2.8D) is chosen as a compromise between good out-of-plane resolution and sufficient distance between the camera and the measurement volume $o_{\min}$. Figure 2a presents $o_{\max}$ and $o_{\min}$ as a function of $\mathcal{F}$ for $c = 23$ μm, which corresponds to 2.3 px for the camera used in this study (Photron mini-WX 100). An f-number of $\mathcal{F} = 11$ provides sufficiently bright images. For $o_f = 5$ m a DOF of $o_{\max} - o_{\min} = L = 4.0$ m can be achieved. As depicted in Fig. 2b for the camera under consideration (Photron mini-WX 100, pixel size: 10 μm) the aforementioned parameters lead to a range of 8 px $< d_G <$ 17 px ($\Delta d_G = 9$ px) for a bubble of diameter $D_B = 10$ mm and 20 px $< d_G <$ 41 px ($\Delta d_G = 21$ px) for a bubble of diameter $D_B = 25$ mm in the measurement volume. Because Δd_G scales approximately linearly with D_G (and therefore D_B) as shown in Eq. (7), a larger bubble will result in better out-of-plane resolution. Assuming a Gaussian peak fit would

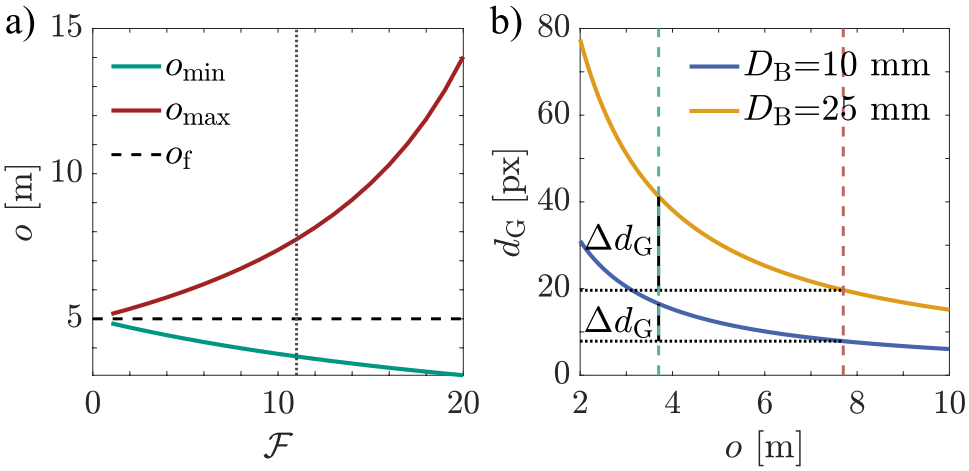

Fig. 2 **a** Depth of field limited by $o_{\min}$ and $o_{\max}$ for varying f-numbers ($\mathcal{F}$) for a constant focus distance $o_f = 5$ m. **b** Image glare-point spacing d_G for bubbles of diameter $D_B \in \{10\text{ mm}, 25\text{ mm}\}$ for different object distances (o) for the set-up with $f = 60$ mm, $\mathcal{F} = 11$, and $o_f = 5$ m for a camera with 10 μm pixel size

provide an approximate accuracy of 0.1 px for the position of the glare-point centre in the image (Raffel et al. 2018), a larger d_G further decreases the uncertainty of the position and velocity reconstruction via Eq. (4).

2.3 Experimental set-up

The measurements are conducted in the 24.0 m × 9.1 m × 9.1 m test section of a large low-speed wind tunnel at the National Research Council in Ottawa, Canada. Figure 3 provides an overview of the experimental set-up. The wake of a 30%-scale tractor-trailer model consisting of a tractor (Kenworth T680 with 1.93 m sleeper) and a trailer (16.15 m dry-van with a height of 1.23 m) is studied. The tractor-trailer model was placed on a 6.1 m-diameter turntable, which was rotated to produce a 9° yaw angle between flow and truck. A measurement volume of approximately 4.0 m × 1.5 m × 1.5 m was assessed by means of the new single-camera set-up. The measurement volume starts from the back of the trailer and extends ∼ 4 m in the x-direction. This placement of the measurement volume allows for the capture of the vortical wake evolving due to the yawed configuration of the trailer.

Two commercial bubble generators (Antari B200) with production rate of ∼ 40 bubble/s each are used. The diameters of the air-filled soap bubbles vary in the range 10 mm $< D_B <$ 25 mm. Both generators are placed ∼ 20 m upstream of the measurement volume in the settling chamber of the wind tunnel at a height $y_b = 4$ m; see Fig. 3a. Two aspects motivate the position of the bubble generators in the settling chamber. First, the position upwind of the contraction (contraction ratio $C = A_s/A_t = 6:1$ between the cross section of the settling chamber A_s and the test section A_t) allows for sufficiently slow wind speeds for the bubble generators to operate within their specifications. Second, the disturbances of the flow introduced by the generator bodies are significantly damped by the time the bubbles have traveled to the measurement volume. Note that the commercial bubble generators used in the present proof-of-concept study are not optimized with regard to aerodynamic shape and seeding output (bubbles per second). Therefore, flow statistic obtained by the present set-up might be biased (influence of the bubble generator wake) and low-seeding densities lead to long measurement times for converged statistics and sparse instantaneous measurements.

Once the soap bubbles enter the measurement volume, they are illuminated by an array of four pulsed high-power LEDs (LED-Flashlight 300, LaVision GmbH) placed in a series configuration, as shown in Fig. 4. The bubble glare points are captured by the main camera A (Photron mini-WX 100, AF Micro-Nikkor 60 mm f/2.8D) with the aperture set to $\mathcal{F} = 11$. To estimate the size of each bubble in the current proof-of-principle study, cameras B and C (Photron SA4, AF Nikkor 50 mm f/1.4D, $\mathcal{F} = 11$, Fig. 4) are added so as

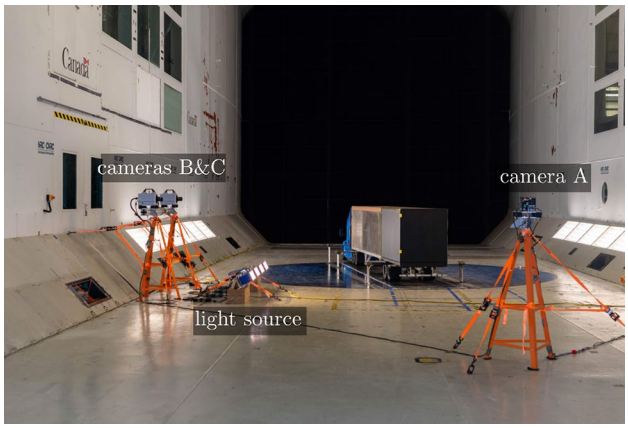

Fig. 4 Image of the experimental set-up taken from the downstream end of the test section

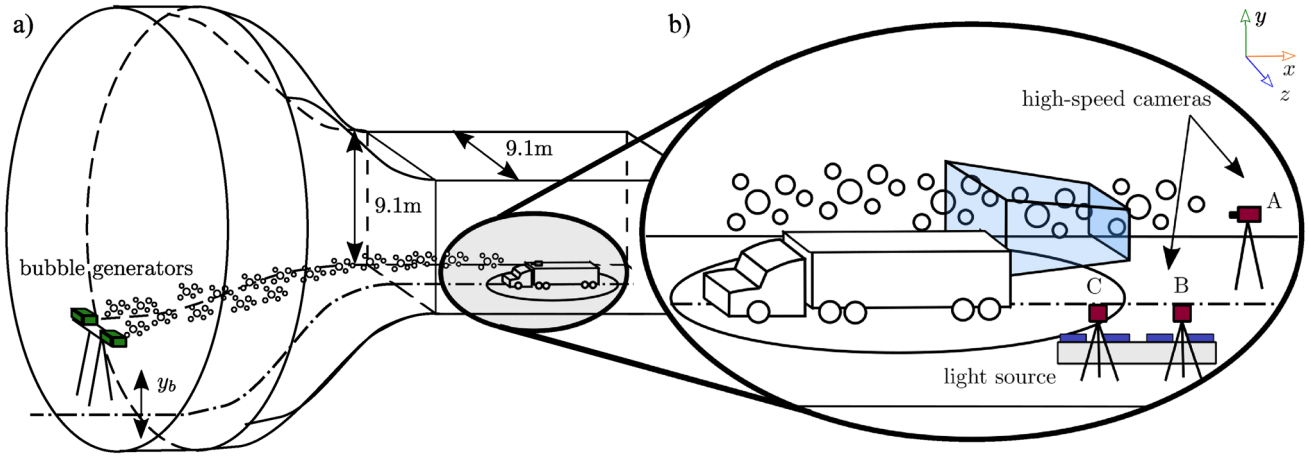

Fig. 3 **a** Sketch of the experimental set-up (not to scale) including the position of the bubble generators (green) in the settling chamber; **b** close-up view of the test section with the measurement volume (light blue), the light source (dark blue), and the cameras (red)

to capture a secondary view to determine the bubble sizes via photogrammetry. Note that this step will not be needed if the bubbles are of known and equal size and is only used here for the bubble-size estimate. Otherwise all steps of the 3D reconstruction are performed only with the data of camera A. A total of 19 runs (5400 images) were collected to assess the wake-flow characteristics at free-stream velocities of $U_\infty = 8$ m/s (3 runs) and $U_\infty = 30$ m/s (16 runs), respectively. Images were recorded at frequencies of $F_{\text{cam}} = 150$ Hz ($U_\infty = 8$ m/s) and $F_{\text{cam}} = 500$ Hz ($U_\infty = 30$ m/s). The cameras were mounted onto the wind-tunnel floor with tripods and vibration-damping camera mounts. The tripods were then fixed with multiple lashing straps as shown in Fig. 4.

2.4 Reconstruction of 3D bubble position

This section describes the detailed processing steps to extract 3D tracks from the set-up as described in Sect. 2.3.

In particular at high wind speeds, the shell of the wind tunnel vibrates at frequencies within the range of 9–40 Hz. While the tractor-trailer model is mounted on the non-vibrating turntable, the cameras experienced significant vibrations. To correct for the vibrations during image processing, non-vibrating reference points were placed in the measurement volume. For camera A, two yellow stickers were attached to the left edge at the back of the trailer (see Fig. 4). For cameras B and C stickers were attached to the opposite wind-tunnel walls. As the first step of processing, the raw images are stabilized (translation and rotation) through cross-correlation of the sticker positions throughout the time series (Fig. 5a, b). Thereafter, the glare points are tracked using standard two-dimensonal PTV (DaVis 8.4.0, LaVision GmbH). An example of the two-dimensional vector map is presented in Fig. 5c.

Subsequently, the two glare-point tracks originating from the same bubble are paired; see Fig. 5d. The pairing is based on a series of conditions. First, the paired tracks have to be reasonably close and their velocities have to be similar. Second, the position of the light source determines the relative orientation of the individual glare points of the same bubble. After the pairing, the temporal evolution of the glare-point spacing ($d_G(t)$) can be extracted. To reduce measurement noise, $d_G(t)$ is smoothed by applying a third-order polynomial fit; see Fig. 5e. For the current proof-of-principle study a constant-diameter bubble generator was not yet available. Therefore, photogrammetry is used to estimate the bubble size (D_B) of a bubble once it appears in the FOV. In particular, the bubble tracks of camera A are matched with the second perspective (cameras B and C) via triangulation. The hereby reconstructed bubble location provides the object distance o of the bubble to camera A. Extracting d_G from the respective image of camera A allows to obtain $D_G = \frac{o d_G}{f}$ (see Eq. (4)) and subsequently $D_B = \sqrt{2} D_G$ (see Eq. (2)). Once D_B is known the second perspective is disregarded and the complete 3D-track is reconstructed from a single view. With equally sized bubbles generated, the former step as shown in Fig. 5f will be redundant. With known D_B, for camera A the object distance (o) of each bubble can be estimated from the glare-point spacing (d_G) in Eq. (2). All cameras are

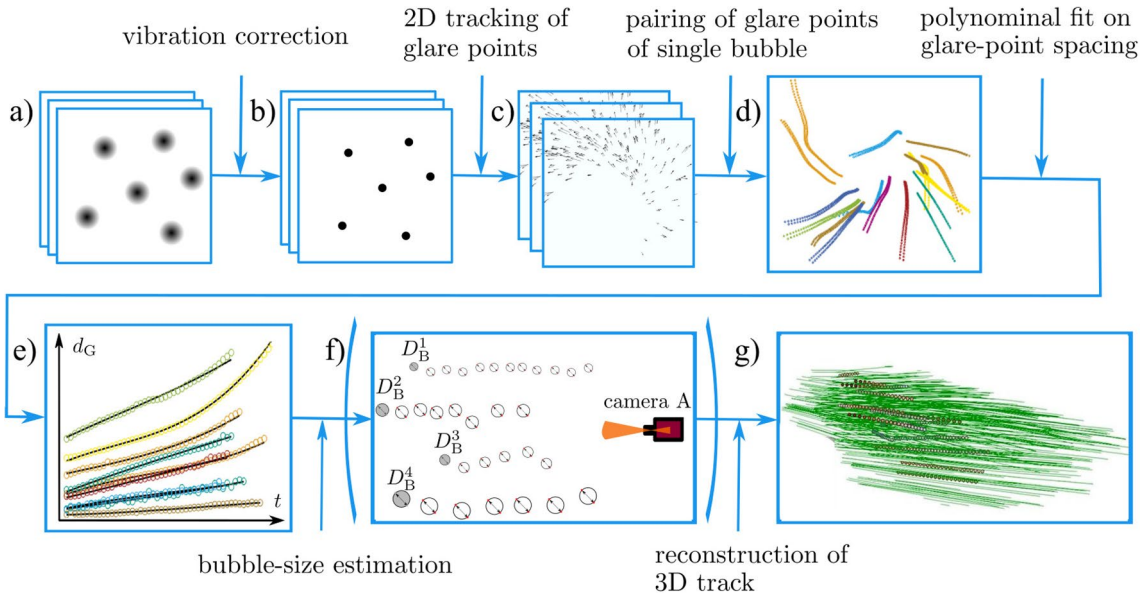

Fig. 5 Diagram outlining the processing steps for computing the 3D tracks from 2D bubble images: **a** raw data; **b** vibration-corrected data; **c** glare-point tracks; **d** location of each paired bubble as a function of time; **e** smoothed glare-point spacing; **f** optional step to estimate bubble size; and **g** reconstructed 3D tracks of bubbles

calibrated by the method suggested by Zhang (2000), providing both the internal camera matrix I and the external matrix $E = (R|T)$ consisting of the rotation matrix R and the translation vector T. The calibration maps the coordinates (x, y, z) from the real-world coordinate system to the frame of reference of the camera chip (X, Y)

$$\begin{bmatrix} X \\ Y \\ m \end{bmatrix} = IE \begin{bmatrix} x \\ y \\ z \\ 1 \end{bmatrix} = IR \begin{bmatrix} x \\ y \\ z \end{bmatrix} + T = I \begin{bmatrix} x_c \\ y_c \\ z_c = o \end{bmatrix}, \tag{8}$$

where m is initially unknown. For sake of clarity, we introduce a second real-world coordinate system with the coordinates (x_c, y_c, z_c) that shares the origin and orientation of the coordinate system of camera A. Since $z_c = o$ is then known, Eq. (8) provides (x_c, y_c, z_c), which then by translation (T) and rotation (R) leads to (x, y, z), and thereby the three-dimensional tracks presented in Fig. 5g.

3 Results

3.1 Statistical analysis of Lagrangian tracks

A total of 5718 bubble tracks were extracted from 3 runs at 8 m/s, and 21534 tracks from 16 runs at 30 m/s. The relatively low number of tracks results from the limited output of the seeding generators used in the present experiment. The higher amount of bubbles per run for the low-speed experiments is due to the longer measurement time (lower camera frequency but the same amount of images per run) in combination with a constant bubble production rate of the bubble generators. The long axis of the measurement volume ($L = 4.0$ m) is aligned with the streamwise direction. Therefore, a maximum number of samples per track (maximum track length) of $n_\infty = F_{\text{cam}} L / U_\infty$ ($n_\infty = 67$ for $U_\infty = 30$ m/s and $n_\infty = 75$ for $U_\infty = 8$ m/s) are expected. Figure 6 presents the distribution of the track lengths (n). The Lagrangian tracks consist of $12 < n < 90$ samples and $12 < n < 80$ samples at $U_\infty = 8$ m/s and at $U_\infty = 30$ m/s, respectively. The very long tracks ($n > n_\infty$) result from the velocity deficit in the wake of the trailer, where $u_x < U_\infty$.

3.2 Vortex wake of tractor-trailer model

Figure 7 presents the pathlines extracted from a single run at $U_\infty = 30$ m/s. The visualization is colour-coded by the streamwise velocity and captures the vortex evolving from the top-right edge of the trailer. The bubbles enter the measurement volume approximately at the end of the trailer and subsequently undergo a twisting motion due to the vortical structure in the wake of the trailer. The reconstructed trajectories presented in Fig. 7 do not represent an instantaneous flow field but the accumulation of pathlines over 10.8 s of measurement time. Therefore, temporal fluctuations of the streamwise velocity u_x are apparent. A lack of bubbles in the lower-left corner of the measurement volume motivates that local seeding would be required to capture the full wake dynamics. In addition, few to no bubbles were tracked in the vortex core. A closer look at the recorded images reveals that the bubbles near the vortex centre experience significant deformation and/or bursting due to large pressure gradients and strong shear on the trailer edge. Going outwards from the vortex centre, the bubble density initially increases and then decreases again. The nonuniform distribution results in part from nonuniform seeding. In addition, the bubble size was estimated by photogrammetry, implying that bubbles that do not appear in the field of view of camera B or C are not included in Fig. 7.

While the extracted Lagrangian data allow for direct determination of material accelerations, material transport, and the identification of coherent structures, the low tracer density of the present proof-of-principle study (only two bubble generators used) does not allow one to extract spatial gradients in the time-resolved data set. In the

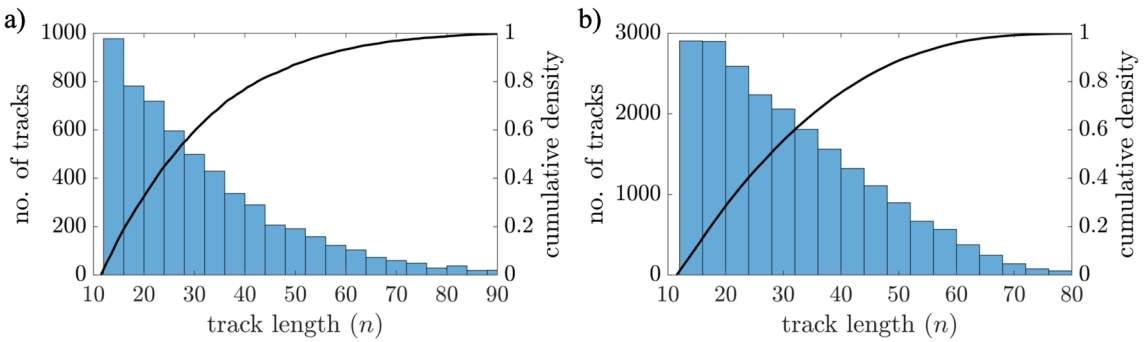

Fig. 6 Track-length distribution of camera A: **a** $U_\infty = 8$ m/s (3 runs); and **b** $U_\infty = 30$ m/s (16 runs). As the bubble generators produce bubbles at a constant rate, testing at the higher wind-tunnel speed of $U_\infty = 30$ m/s results in fewer recorded tracks per run

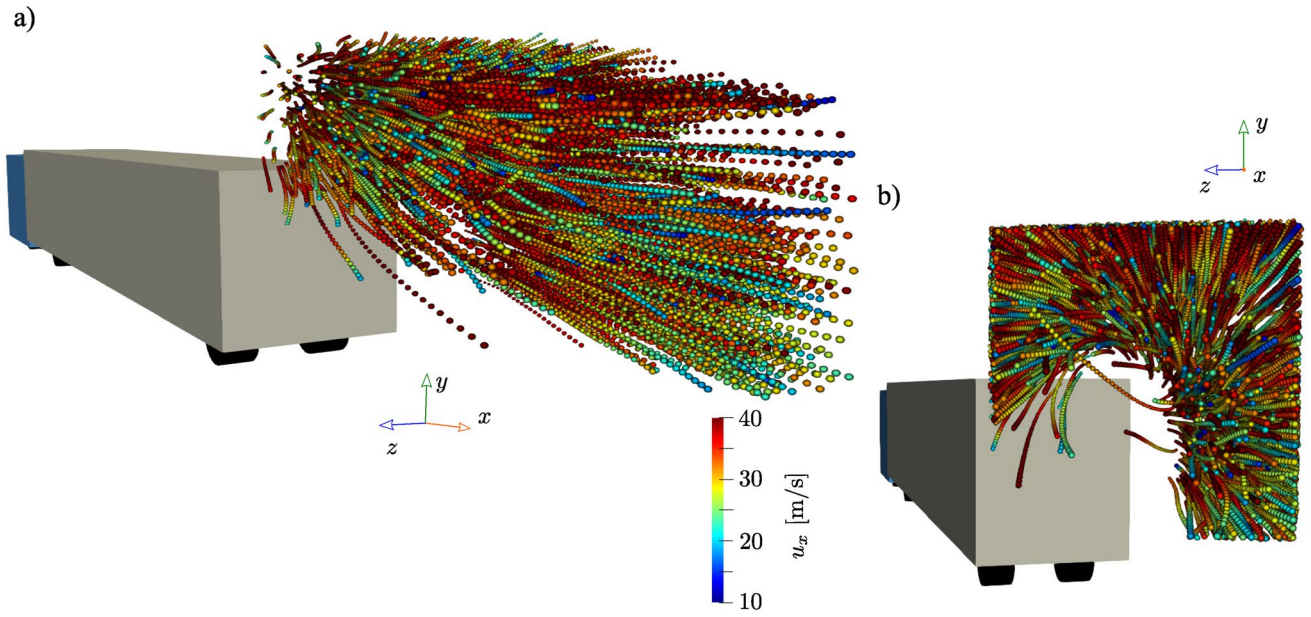

Fig. 7 A total of 2774 reconstructed bubble tracks at $U_\infty = 30$ m/s. The tracks are obtained at various time instances during a single run in 10.8 s and therefore do not represent an instantaneous snapshot of the flow: **a** isometric view of the tracks; **b** back-view from camera A, displaying the vortical wake

following, the data are mapped on an Eulerian grid and averaged over time. A uniform $80 \times 30 \times 30$ grid with a resolution of 0.05 m is defined and for each grid point the data are averaged. The mapping of the data to an equidistant Eulerian grid allows the visualization of the mean velocity field, streamlines, as well as an estimate of the vorticity distribution. Figure 8a shows the in-plane velocity at different streamwise locations in the wake colour-coded by its magnitude $\left(\sqrt{u_y^2 + u_z^2}\right)$. Again, the streamwise vortex is apparent and a large velocity magnitude in the negative y-direction can be observed behind the truck. While no bubbles are present in the immediate vortex core itself, significant streamwise vorticity (ω_x) can be observed in close vicinity, as depicted in Fig. 8b.

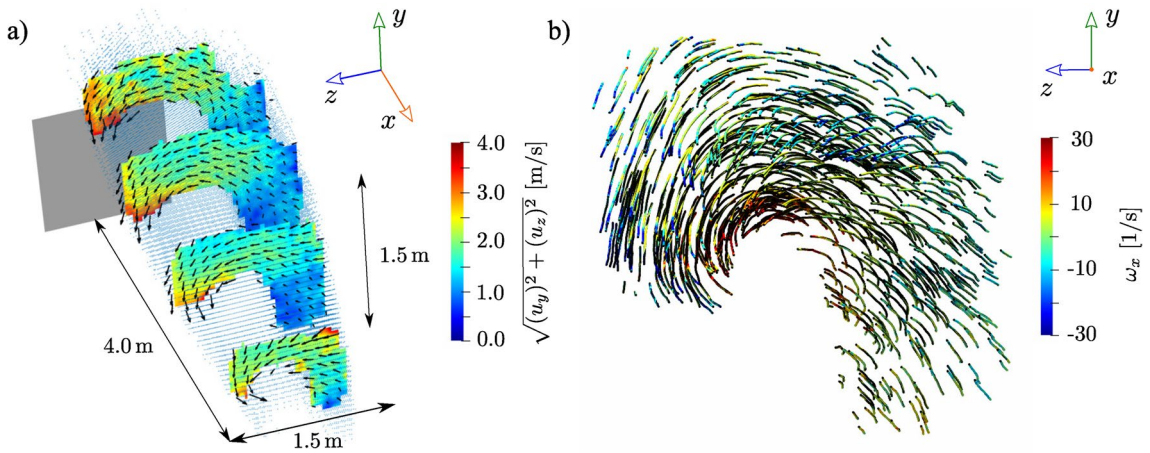

Fig. 8 Averaged velocity data at $U_\infty = 30$ m/s: **a** in-plane velocity visualized by direction (black vectors) and magnitude (contour plot) in four planes at different streamwise locations behind the truck (grey). The equidistant Eulerian grid (spacing 0.05 m) is visualized by blue dots. **b** Streamlines from the perspective of camera A, and colour-coded by streamwise vorticity

4 Conclusions

The present manuscript introduces a novel method for 3D particle tracking over large volumes that enables affordable and efficient measurements using a single camera and white light. The technique relies on tracking glare points of centimeter-sized soap bubbles. The depth of the soap bubbles is determined from the glare-point spacing in the image space. After outlining the fundamental equations that enable the 3D reconstruction from a single view, the optical parameters of such a set-up are discussed, and suggestions for the selection of the focal length (f) and the f-number ($\mathcal{F}$) are provided. In addition, a series of post-processing methods is presented that provides the 3D tracks from the images of a single camera.

As a proof-of-concept, the new method is then tested in a large, low-speed wind tunnel by extracting the wake of a tractor-trailer model. A large measurement volume ($V = \mathcal{O}(10\,\mathrm{m}^3)$) is captured with a high-resolution camera (2048 px × 2048 px). The flow is seeded with two commercial bubble machines producing bubbles of diameter in the range of $10\,\mathrm{mm} < D_B < 25\,\mathrm{mm}$. Without bubble generators that produce bubbles of uniform and known size, the bubble size (D_B) needs to be determined for each bubble. If the position of a bubble is known at a single time instant along its path, the bubble size can be estimated as $D_B = \frac{\sqrt{2} o d_G}{f}$ (Eq. (4)). Possible implementations of this principle include placing the bubble generator at a known position in the FOV, estimating the bubble size once the bubble enters the illuminated area, or recording the flow from a second perspective to determine D_B via photogrammetry. In the present experiment, photogrammetry was used to provide a reliable and accurate estimate of D_B. Once D_B is determined, the glare-point spacing allows to reconstruct the 3D position of each bubble along its complete path from a single perspective. Despite the challenging environment of the large-scale wind tunnel (vibrations, issues with accurate alignment due to long distances, etc.) along with non-ideal seeding (low seeding density, narrow seeding area) the novel approach proved to be successful. Time-resolved Lagrangian data as well as 3D time-averaged velocity fields were extracted.

In comparison with traditional multi-camera approaches, the novel method comes with several benefits but also major drawbacks. The easy, robust, safe, and affordable set-up of the new glare-point approach allows large measurement volumes but comes at the expense of decreasing measurement accuracy. However, motivated by the present proof-of-concept study, the three major issues that compromise the accuracy (and the effort) of the one-camera approach will be mitigated in the future: (1) the limited tracer fidelity due to the non-Stokesian behaviour of the bubbles can be addressed by models that correct the measured tracks; (2) the amount of pixels in the limited out-of-plane resolution (Δd_G) directly depends on the pixel size, which continuously decreases as in the field of camera development advances; and (3) custom and aerodynamically-optimized bubble generators that produce uniformly-sized bubbles can replace the seeding generators used in the present study. Future investigations will focus on modelling the non-Stokesian behaviour of the tracers and the seeding generator optimization.

Acknowledgements The authors thank LaVision GmbH for loaning 3 of 4 pulsed LED arrays, and Dr. Brian McAuliffe at National Research Council Canada (NRC Canada) for providing access to the 9m wind tunnel. Furthermore, the authors thank the team of the 9m wind tunnel for continuous support during the measurement campaign.

References

Bosbach J, Schanz D, Godbersen P, Schröder A (2019) Dense Lagrangian particle tracking of turbulent Rayleigh Bénard convection in a cylindrical sample using Shake-The-Box. In: 17th European turbulence conference (ETC 2019), Deutsches Zentrum für Luft- und Raumfahrt eV, vol 631, pp 1–1

Buchmann NA, Willert CE, Soria J (2012) Pulsed, high-power LED illumination for tomographic particle image velocimetry. Exp Fluids 53(5):1545–1560

Cierpka C, Kähler CJ (2012) Particle imaging techniques for volumetric three-component (3D3C) velocity measurements in microfluidics. J Vis 15(1):1–31

Clift R, Grace JR, Weber ME (1978) Bubbles, drops, and particles. Academic Press, New York

Dehaeck S, van Beeck JPAJ, Riethmuller ML (2005) Extended glare point velocimetry and sizing for bubbly flows. Exp Fluids 39(2):407–419

Elsinga GE, Scarano F, Wieneke B, van Oudheusden BW (2006) Tomographic particle image velocimetry. Exp Fluids 41(6):933–947

Fahringer TW, Lynch KP, Thurow BS (2015) Volumetric particle image velocimetry with a single plenoptic camera. Meas Sci Technol 26(11):115201

Galler J, Rival DE (2019) Inverse technique for Lagrangian, non-Stokesian tracer particle correction. In: 13th International symposium on particle image velocimetry, July 22–24, 2019, Munich, Germany

Gao Q, Wang HP, Wang JJ (2012) A single camera volumetric particle image velocimetry and its application. Sci China Technol Sci 55(9):2501–2510

Greenleaf AR (1950) Photographic optics. Macmillan, New York

Huhn F, Schanz D, Gesemann S, Dierksheide U, van de Meerendonk R, Schröder A (2017) Large-scale volumetric flow measurement in a pure thermal plume by dense tracking of helium-filled soap bubbles. Exp Fluids 58(9):116

Jux C, Sciacchitano A, Schneiders JFG, Scarano F (2018) Robotic volumetric PIV of a full-scale cyclist. Exp Fluids 59(4):74

Kao HP, Verkman AS (1994) Tracking of single fluorescent particles in three dimensions: use of cylindrical optics to encode particle position. Biophys J 67(3):1291–1300

Kornek U, Müller F, Harth K, Hahn A, Ganesan S, Tobiska L, Stannarius R (2010) Oscillations of soap bubbles. New J Phys 12(7):073031

Kurada S, Rankin GW, Sridhar K (1995) A trinocular vision system for close-range position sensing. Opt Laser Technol 27(2):75–79

Maas HG, Gruen A, Papantoniou D (1993) Particle tracking velocimetry in three-dimensional flows. Exp Fluids 15(2):133–146

Michaux F, Mattern P, Kallweit S (2018) RoboPIV: How robotics enable PIV on a large industrial scale. Meas Sci Technol 29(7):074009

Nishino K, Kasagi N, Hirata M (1989) Three-dimensional particle tracking velocimetry based on automated digital image processing. J Fluids Eng 111(4):384–391

Raffel M, Willert CE, Scarano F, Kähler CJ, Wereley ST, Kompenhans J (2018) Particle image velocimetry: a practical guide, 3rd edn. Springer Verlag, Berlin

Rosi GA, Rival DE (2018) A Lagrangian perspective towards studying entrainment. Exp Fluids 59(1):19

Rosi GA, Sherry M, Kinzel M, Rival DE (2014) Characterizing the lower log region of the atmospheric surface layer via large-scale particle tracking velocimetry. Exp Fluids 55(5):1736

Scarano F (2012) Tomographic PIV: principles and practice. Meas Sci Technol 24(1):012001

Scarano F, Ghaemi S, Caridi GCA, Bosbach J, Dierksheide U, Sciacchitano A (2015) On the use of helium-filled soap bubbles for large-scale tomographic PIV in wind tunnel experiments. Exp Fluids 56(2):42

Schanz D, Gesemann S, Schröder A (2016) Shake-The-Box: Lagrangian particle tracking at high particle image densities. Exp Fluids 57(5):70

Schneiders JFG, Scarano F, Jux C, Sciacchitano A (2018) Coaxial volumetric velocimetry. Meas Sci Technol 29(6):065201

Sellappan P, McNally J, Alvi FS (2018) Time-averaged three-dimensional flow topology in the wake of a simplified car model using volumetric PIV. Exp Fluids 59(8):124

Suryadi A, Ishii T, Obi S (2010) Stereo PIV measurement of a finite, flapping rigid plate in hovering condition. Exp Fluids 49(2):447–460

Toloui M, Riley S, Hong J, Howard K, Chamorro LP, Guala M, Tucker J (2014) Measurement of atmospheric boundary layer based on super-large-scale particle image velocimetry using natural snowfall. Exp Fluids 55(5):1737

van de Hulst HC, Wang RT (1991) Glare points. Appl Opt 30(33):4755–4763

Willert CE, Gharib M (1992) Three-dimensional particle imaging with a single camera. Exp Fluids 12(6):353–358

Zhang Z (2000) A flexible new technique for camera calibration. IEEE Trans Pattern Anal Mach Intell 22(11):1330–1334

Zhao Z, Buchner AJ, Atkinson C, Shi S, Soria J (2019) Volumetric measurements of a self-similar adverse pressure gradient turbulent boundary layer using single-camera light-field particle image velocimetry. Exp Fluids 60(9):141